# Highly Efficient Visible-Light-Driven Photocatalytic Hydrogen Production Using Robust Noble-Metal-Free $Zn_{0.5}Cd_{0.5}S$@Graphene Composites Decorated with $MoS_2$ Nanosheets

*Puttaswamy Madhusudan, Run Shi, Bananakere Nanjegowda Chandrashekar, Shengling Xiang, Ankanahalli Shankaregowda Smitha, Weijun Wang, Haichao Zhang, Xian Zhang, Abbas Amini, and Chun Cheng\**

Solar water splitting using semiconductor photocatalysts is considered to be one of the economical and significant techniques for hydrogen evolution. In this study, graphene–$Zn_xCd_{1-x}S$ (ZCS) heterojunction is fabricated by hydrothermal method followed by simple photodeposition of ultrathin few layers of molybdenum sulfide ($MoS_2$) nanosheets. The results show that compared with pristine ZCS and 1 wt% graphene mixed ZCS photocatalysts, the 1 wt% graphene and 1 wt% $MoS_2$ photodeposited ZCS composited sample shows 39.5 mmol $h^{-1}$ $g^{-1}$ hydrogen production activity, which is 6.9 and 1.9 times significantly higher, respectively, with an apparent quantum yield of 53% at 420 nm visible light is recorded. The improved photocatalytic activity can be attributed to the formation of heterostructure interface between p-type $MoS_2$ nanosheets with n-type ZCS host, which allows for the faster transfer of the photogenerated electrons and thus significantly promotes the separation of photogenerated charge carriers.

## 1. Introduction

The depletion of fossil fuels and drastically increase in global demand for renewable energy has stimulated intense research on sustainable energy conversion, storage, and solar water splitting.[1] Meanwhile, the production of hydrogen and oxygen from water and semiconductor catalysts is considered as a promising means of utilizing solar energy. The main aspect of water splitting is the fabrication of photocatalysts that are stable, cheap, and responsive to visible light, and have high quantum efficiency.[2] In this regard, considerable efforts have been devoted to investigating suitable semiconductor-based photocatalysts and their composites with excellent photocatalytic hydrogen evolution.[3] Although the past couple of decades have witnessed outstanding progress in the efficiency and stability of the catalysts, fundamental issues from the material's perspective are still lingering.[4] Among various photocatalysts, zinc cadmium metal sulfide (ZCS), as an n-type band-gap semiconductor, has been proven to be a general photocatalyst for solar $H_2$ production.[5–7] This is because the band gap of nonstoichiometric $Zn_xCd_{1-x}S$ (ZCS) can be tuned to ≈2.4 eV, which can be easily excited under visible-light irradiation.[8] Nevertheless, the pristine ZCS catalyst suffers greatly from the high recombination rate of photoexcited charge carriers as well as low photocatalytic activity and stability.[9–11] The valence band (VB) of ZCS consists of $S^{2-}$ with a small electronegativity, so the photogenerated holes on the VB are responsible to be self-oxidation other than oxidizing water molecules, resulting in photocorrosion.[12] Hereof, a series of strategies are developed to improve the photocatalytic performance of ZCS, such as doping with metal or nonmetal elements, copolymerization, nanostructuring, constructing different hybrid heterojunctions or composites with other semiconductors or metal–organic frameworks.[13–30] However, achieving efficient and durable charge separation on ZCS-based catalysts is still a significant challenge.

2D carbon-based materials like graphene, graphene oxide (GO), carbon nitride, and holey graphene have emerged as

Dr. P. Madhusudan, R. Shi, Dr. B. N. Chandrashekar, S. Xiang,
A. S. Smitha, W. Wang, H. Zhang, X. Zhang, Prof. C. Cheng
Department of Materials Science and Engineering
Southern University of Science and Technology (SUSTech)
Shenzhen 518055, P. R. China
E-mail: chengc@sustech.edu.cn
Dr. P. Madhusudan, Prof. C. Cheng
Shenzhen Engineering Research and Development Center for Flexible
Solar Cells
Southern University of Science and Technology (SUSTech)
Shenzhen 518055, P. R. China
Dr. P. Madhusudan, Prof. C. Cheng
Guangdong Provincial Key Laboratory of Energy Materials for Electric
Power
Southern University of Science and Technology (SUSTech)
Shenzhen 518055, China
Prof. A. Amini
Center for Infrastructure Engineering
Western Sydney University
Kingswood NSW 275, Australia

The ORCID identification number(s) for the author(s) of this article can be found under https://doi.org/10.1002/admi.202000010.

**ADVANCED
SCIENCE NEWS**
www.advancedsciencenews.com

**ADVANCED
MATERIALS
INTERFACES**
www.advmatinterfaces.de

new photocatalytic materials due to their excellent electronic, optical, physicochemical, and surface properties.[31] Among these numerous carbon-based earth-abundant materials, graphene with unique 2D honeycomb structure, superior mechanical and electrical properties, specific $\pi$-conjugation structure, large specific surface area, and high conductivity offers a good opportunity to fabricate graphene–metal sulfide composites as photocatalysts for water splitting.[32] Although considerable progress has been made to enhance the photocatalytic activity of graphene–ZCS, most of these efforts still need noble metals co-catalysts to enhance $H_2$ production.[33] Therefore, it is very essential to develop nonexpensive earth-abundant co-catalysts clustered graphene–ZCS based photocatalysts without noble metal loading.
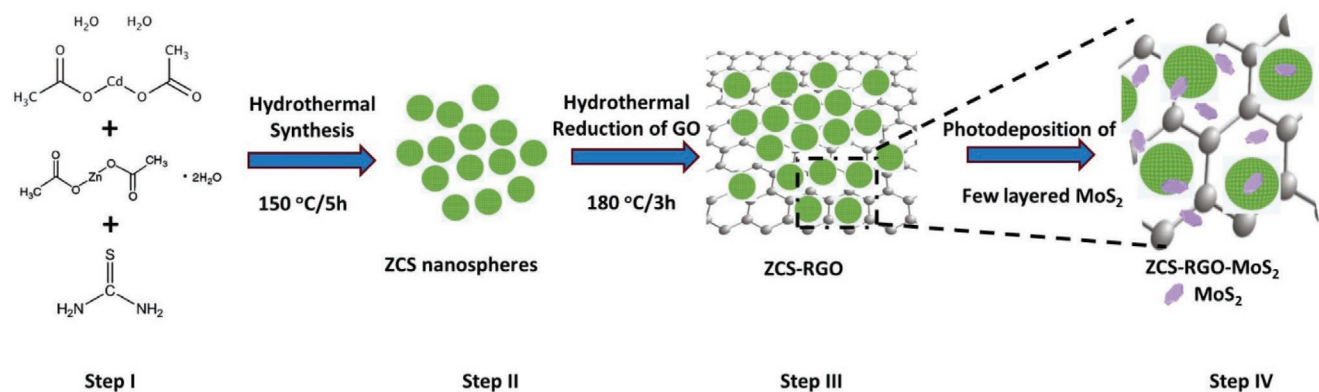
Molybdenum sulfide ($MoS_2$) as a p-type semiconductor with a layered structure and comprising inexpensive and earth-abundant elements has gained a lot of interest recently due to its unique optoelectronic properties and potential applications in water splitting.[34] $MoS_2$ has also been reported as an efficient co-catalyst on a variety of semiconductor photocatalysts.[35,36] For instance, Wong et al. found that 3 wt% loading $MoS_2$ as a co-catalyst onto ZCS via a photoassisted deposition approach using $(NH_4)_2MoS_4$ as a precursor showed 0.42 mmol $h^{-1}$ $g^{-1}$ of $H_2$ generation, which is 210 times faster $H_2$ evolution rate on visible-light illumination compared with that obtained for pristine $Zn_{0.2}Cd_{0.8}S$ photocatalyst (0.002 mmol $h^{-1}$ $g^{-1}$). They proposed that the in situ photodeposited few-layered $MoS_2$ onto the $Zn_{0.2}Cd_{0.8}S$ surface played a key role in improving the photocatalytic activity, thus forming a thin-layered heterogeneous nanojunction.[37] Similarly, Tu et al. prepared a $Zn_{0.5}Cd_{0.5}S$ solid solution through the hydrothermal method subsequently loading a suitable amount of $MoS_2$ nanosheets to enhance the photoactivity. The maximum $H_2$-production activity of 12.30 mmol $h^{-1}$ $g^{-1}$ was obtained under visible-light irradiation from an aqueous solution of lactic acid.[38] But, the method they had adopted suffered from stability and only a moderate increase to good $H_2$ evolution. Furthermore, most of the ZCS solid solutions clustered with co-catalysts show unsatisfying catalytic activity in water splitting for $H_2$ evolution under visible light or either co-doped with noble metals.[39–44] Despite some of the noble metal doped ZCS catalysts exhibited high photocatalytic activity, they did not show satisfactory recycling stability, thus restricting their potential application.[45,46] Therefore, the development of p-graphene-n (p-g-n) heterojunction with significantly enhanced catalytic activity and long-term durability is highly desirable. Although, such heterojunction was initially designed by Guo et al. where both RGO and $MoS_2$ were instantaneously reduced under UV light irradiation resulting in numerous defects in ZCS and RGO interfaces that moderate improved photocatalytic activity involving lactic acid as a sacrificial reagent.[47] But, in the above-mentioned case, $H_2$ evolution under visible light was not very convincing. However, to our knowledge, there is no research on CZS hollow nanosphere's solid-solution photocatalyst coupled with p-g-n heterojunction displaying improved $H_2$ production. Hence, there is substantial scope for further organized research on budget-friendly ZCS based p-g-n system to boost the overall visible-light-driven water splitting with better durability and improved photocatalytic $H_2$ evolution reaction.

In the present work, two-step preparation methods were employed to fabricate in situ photodeposition of few-layer $MoS_2$ nanosheets over the graphene–ZCS photocatalysts using $(NH_4)_2MoS_4$ aqueous solution as a precursor. The as-prepared p-g-n heterojunction catalysts show significantly enhanced photocatalytic activity for hydrogen evolution in the presence of $Na_2S$ and $Na_2SO_3$ sacrificial reagents under visible-light irradiation. The improved photocatalytic activity can be attributed to the intimate interfacial close contact between p-type $MoS_2$ and graphene nanosheets with n-type ZCS heterostructures, which can facilitate the effective transfer and separation of the photoinduced charge carriers. The presence of $MoS_2$ nanosheets in graphene–ZCS heterojunction extends its visible-light response to longer wavelength and also reduces the photocorrosion of the ZCS catalyst. The resulting noble metal-free $MoS_2$ coupled graphene–ZCS heterojunction shows higher photocatalytic activity than pure ZCS and graphene–ZCS prepared under the same experimental condition. Furthermore, the hydrogen production rate of 1 wt% platinum doped graphene–ZCS is relatively lower than our optimized catalyst, that is 1 wt% graphene and 1 wt% $MoS_2$ photodeposited ZCS composited sample (1M-ZCSG1), indicating our 1M-ZCSG1 is an effective noble metal-free catalyst. The as-prepared in situ photodeposited $MoS_2$ over graphene–ZCS composites is relatively stable even after five consecutive repetitive cycles with remarkable enhanced $H_2$-production activity. The present work demonstrates that coupling few layers of $MoS_2$ over graphene with ZCS hollow nanospheres is an efficient way to promote catalytic activity, which may be useful in the design of other visible-light responsive photocatalysts.

## 2. Results and Discussion

ZCS hollow nanospheres were prepared by a simple hydrothermal method using zinc and cadmium acetate along with thiourea. Further, we prepared graphene–ZCS heterojunction at the third step. Finally, $MoS_2$ nanosheets were photodeposited onto the surface of the graphene–ZCS nanoheterojunctioned sample that was achieved at the fourth step (**Scheme 1**). The detailed synthetic procedures are described in the Experimental Section.

X-ray diffraction (XRD) was utilized to obtain information about the phase purity of the synthesized materials. As shown in Figure S1† (Supporting Information) the diffraction peaks, corresponding to graphene–ZCS, with different graphene content significantly left-shift compared to the standard diffraction of ZnS and CdS demonstrating that the obtained heterojunctions are not a mixture of ZnS and CdS, but ZCS solid solution. The diffraction pattern of ZCS sample shows typical hexagonal wurtzite and cubic structures with several prominent peaks, which are indexed to (100), (002), (101), (110), (103), (112), and (202) planes of ZCS wurtzite phase, while the crystal planes (111), (200), and (311) correspond to ZCS cubic phase. No diffraction peaks of impurities can be observed, which indicates the high phase purity of the as-prepared samples. The corresponding ZCS's diffraction peaks in graphene–ZCS samples correspond to ZCS, and are sharp and intense, signifying that the phase of ZCS is not significantly changed even after

**ADVANCED
SCIENCE NEWS**

www.advancedsciencenews.com

**ADVANCED
MATERIALS
INTERFACES**

www.advmatinterfaces.de

**Scheme 1.** Schematic illustration of the deposition of few layered $MoS_2$ nanosheets over graphene–ZCS hollow nanospheres. Step I: Mixing of starting reagents. Step II: Formation of ZCS nanospheres using hydrothermal method at 150 °C/5 h. Step III: Hydrothermal reduction of graphene over ZCS nanospheres at 180 °C/3 h. Step IV: Photodeposition of $MoS_2$ nanosheets over ZCS–RGO composites.

the introduction of different amount of graphene nanosheets. No characteristic diffraction peaks of graphene and $MoS_2$ can be observed in the diffraction patterns of the as-prepared $MoS_2$–graphene–$Zn_{0.5}Cd_{0.5}S$ (XM-ZCSG1) samples because of their slow amount and relatively low diffraction intensity (see **Figure 1**). Note that, similar synthesis procedures were employed in previous studies to fabricate CdS nanostructures co-doped with different amounts of $MoS_2$ suggesting no diffraction peaks could be observed due to the low content and high dispensability of $MoS_2$ nanosheets.[48] However, graphene and $MoS_2$ were easily observed through high-resolution transmission electron microscopy (HRTEM), scanning transmission electron microscopy (STEM) mapping, X-ray photoelectron spectroscopy (XPS) analysis, and Raman spectroscopy.

The nitrogen adsorption–desorption isotherms and the corresponding pore-size distribution curves (inset) for the ZCS, ZCSG1, and 1M-ZCSG1 samples are shown in Figure S2† (Supporting Information). The ZCSG1 and 1M-ZCSG1

samples have similar isotherms and pore-size distributions of type IV (Brunauer–Deming–Deming–Teller classification) isotherms with an H3 hysteresis loop, signifying the presence of slit-like pores.[49] At low relative pressures (below 0.2), the isotherms exhibit a relatively high absorption, suggesting the presence of several micropores. Besides, the high adsorption in the relatively high-pressure range (approaching 1.0) indicates the presence of large mesopores and macropores.[50] The bi-model pore-size distribution curves are calculated from the desorption branch of the nitrogen isotherms based on the Barrett–Joyner–Halenda (BJH) method. The bi-model pores are attributed due to intra-aggregated pores formed by graphene and large inter-aggregated pores formed within the ZCS nanospheres decorated over the graphene nanosheets. The corresponding pore-size distribution (inset) indicates a wide distribution ranging from 2 to over 100 nm with peak pore diameters at 3.5 and 88.5 nm, respectively. It is presumed that the porous structures of these composite materials are extremely useful in photocatalysts as they provide efficient transport pathways of reactant molecules and products.[51] The Brunauer–Emmett–Teller (BET) surface areas, pore volumes, and average pore diameter of as-prepared composite samples are listed in Table S1† (Supporting Information).

The morphologies of ZCS and 1M-ZCSG1 samples were analyzed by field emission scanning electron microscopy (FESEM) to evaluate the structure of ZCS and the influence of graphene and $MoS_2$ nanosheets on the morphology of ZCS nanospheres. The FESEM micrograph in **Figure 2**a shows monodispersed ZCS nanospheres with an average diameter of ≈100–120 nm with their external rough surface composed of loosely arranged interconnected tiny primary nanoparticles (10–20 nm in size) (see Figure 2a, inset) within the nanospheres. In contrast, Figure 2b (1M-ZCSG1 sample) shows uniformly decorated ZCS nanospheres on the exfoliated near-transparent graphene sheets, indicating that graphene may act as a host to hold ZCS nanospheres. Suspended graphene sheets can be distinguished by the observation of blurry contrast as marked by arrows. Besides, it has been reported previously that nanoparticles may interact with graphene sheets through physicabsorption, electrostatic binding, and charge transfer interaction, thus enhanced the charge separation and higher photocatalytic
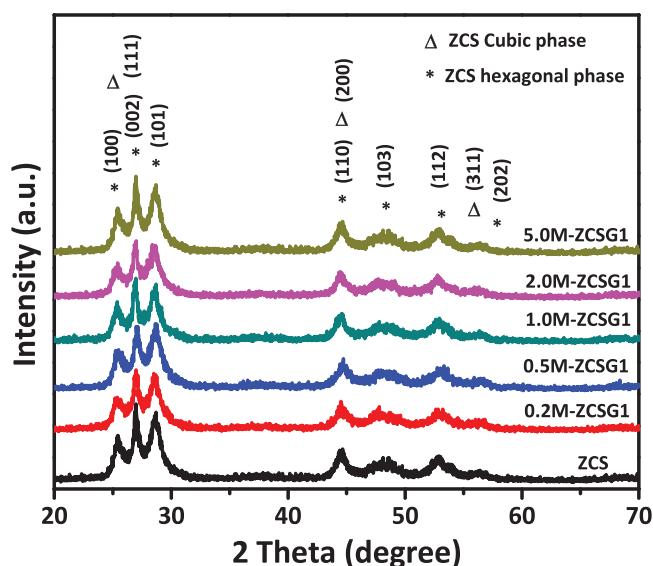


**Figure 1.** XRD pattern of ZCS and XM-ZCSG1 heterojunctions with different weight percent of $MoS_2$ nanosheets.
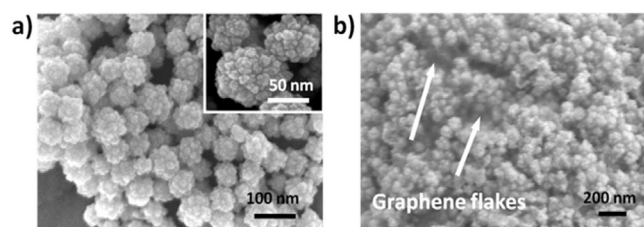
**Figure 2.** a) FESEM images of ZCS hollow nanospheres; the inset shows a high magnification image, indicating a ZCS nanospheres surface consisting of many nanoparticles b) FESEM image of 1M-ZCSG1 sample.

efficiency.[52] Furthermore, it is significant to mention, no specific morphology of $MoS_2$ could be resolved in the FESEM image indicating a few layers of $MoS_2$ nanosheets grown in the composite sample. It is believed that the few-layered $MoS_2$ nanosheets grown by the simple photodeposition could not be distinguished in the FESEM image.[48] The energy-dispersive X-ray spectroscopy (EDS) spectrum of the 1M-ZCSG1 sample in Figure S3† (Supporting Information) clearly illustrates that the chemical composition consists of Zn, Cd, S, C, and Mo elements. The Al peak originates from the sample analysis grid. The above EDS results further confirm the presence of $MoS_2$ nanosheets and phase purity of as-prepared composite catalysts. Atomic force microscopy (AFM) characterization was carried out on a 1M-ZCSG1 sample and is shown in Figure S4† (Supporting Information) where graphene nanosheets with lateral size of several micrometers were observed surrounded by ZCS nanospheres. The corresponding height profile of a graphene nanosheet shows a thickness of 4 nm. This result directly indicates ultrathin graphene acts as a template for anchoring ZCS nanospheres.

The detailed morphologies and components of as-prepared samples were investigated by transmission electron microscopy (TEM). Figure S5† (Supporting Information) shows a typical ZCS nanosphere, from the image it would be seen that the strong contrast between the dark edge and pale center suggests hollow nature of as-prepared ZCS nanospheres. **Figure 3**a shows uniform ZCS hollow spheres with a diameter range of 100–130 nm. Further, ZCS nanospheres are adhered over the nearly transparent exfoliated graphene flakes. Interestingly, the outer surface of ZCS nanospheres consisted of small pores with a size of several nanometers; such pores make ZCS highly permeable for efficient mass transport. The porous

structure of ZCS is consistent with the result of N2 sorption measurement (Figure S2†, Supporting Information), in which a peak centered at 3 nm is observed. Due to the lower dispersion and intergrowth over graphene and ZCS as well as low contrast, photodeposited few-layered $MoS_2$ nanosheets could not be distinguished in the low magnification TEM image. The photocatalytic activity of hollow ZCS composites is presumed to be much better than that of ZCS particles. Besides, the interior structure of ZCS hollow nanospheres could allow multiple reflections of visible light within the interior cavities and benefit electrons and holes transportation and separation. Figure 3b shows the HRTEM image of 1M-ZCSG1, in which three types of intimately contacted lattice fringes were observed, confirming heterojunction formation between ZCS, graphene, and $MoS_2$. Besides, the enlarged HRTEM images in Figure 3b with number 1 and 2 represent lattice fringes of ZCS and $MoS_2$, respectively. The well-developed lattice fringes of 0.32 nm are assigned to the interplanar distance of (002) crystallographic planes in hexagonal ZCS, while the lattice spacing of 0.62 nm corresponds to the (002) plane of hexagonal $MoS_2$ nanosheets. Furthermore, the smooth graphene layer conforms to a highly conductive layer over the surface of ZCS and $MoS_2$ nanosheets. It can be noted that the (002) plane of $MoS_2$ comprises few layers of $MoS_2$ nanosheets illustrating the in situ photodeposition of $MoS_2$ over the graphene nanosheets. Furthermore, the above high magnification HRTEM results manifest the intimate contact is formed between ZCS, graphene, and $MoS_2$
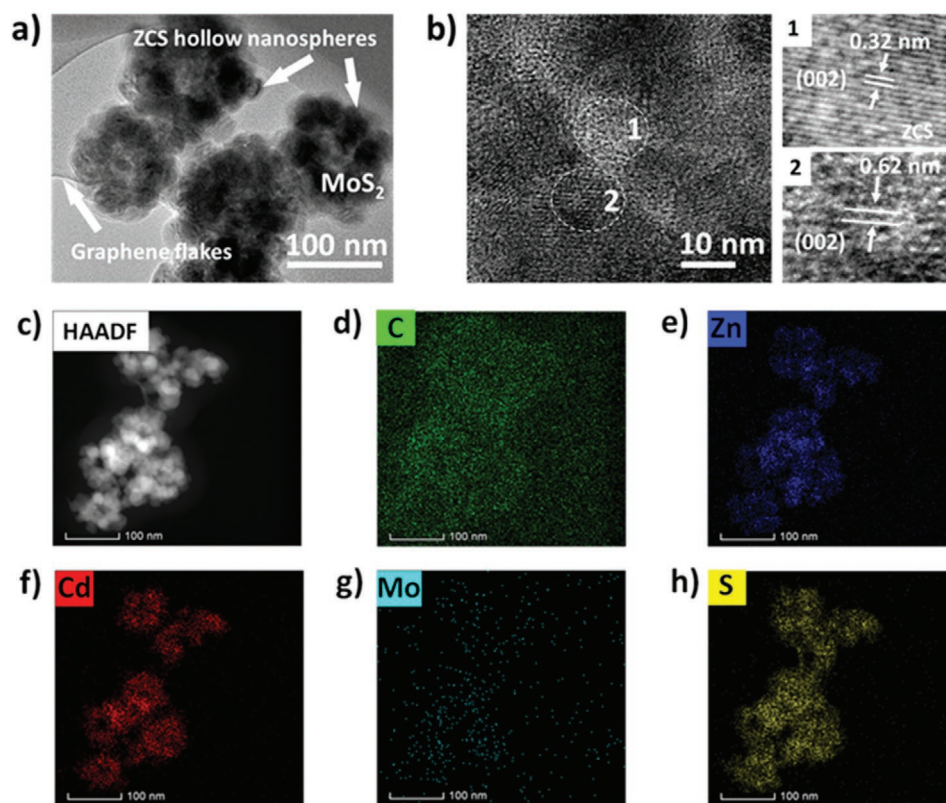


**Figure 3.** a) TEM and b) HRTEM images where 1 and 2 show lattice fringes of ZCS and $MoS_2$, respectively. c) The selected area for STEM element mappings, d–h) for elements Zn, Cd, Mo, S, and C, respectively, of as-prepared 1M-ZCSG1 heterojunctions.
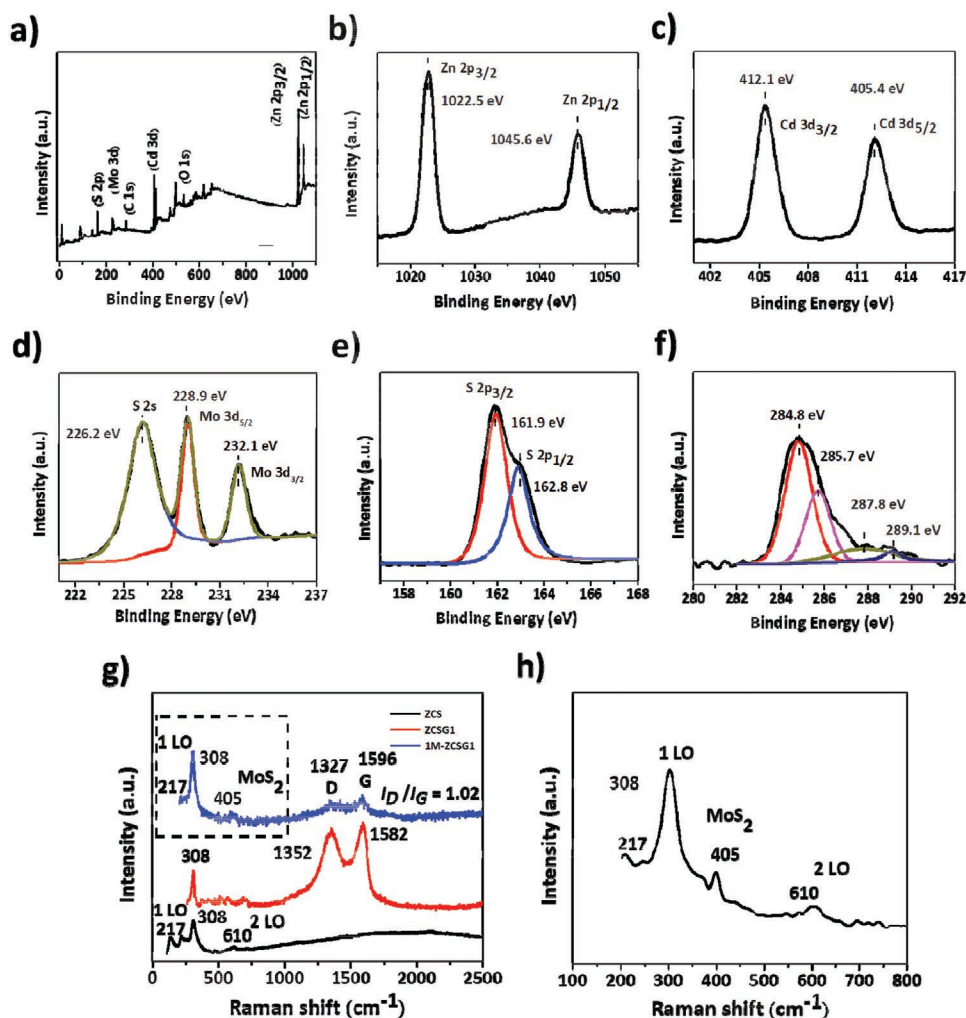
**ADVANCED
SCIENCE NEWS**

www.advancedsciencenews.com

**ADVANCED
MATERIALS
INTERFACES**

www.advmatinterfaces.de

**Figure 4.** a) Typical XPS survey spectra, b) high-resolution XPS spectra of Zn 2p region, c) Cd 3d region, d) Mo 3d region, e) S 2p region, and f) C 1s region in 1M-ZCSG1 sample. g) Raman spectra of ZCS, ZCSG1, and 1M-ZCSG1 samples. h) Selected area enlarged view of 1M-ZCSG1 sample showing $MoS_2$ presence.

favoring the electron transfer from ZCS to graphene to $MoS_2$. Figure 3c shows the high-angle annular dark-field STEM image of a typical 1M-ZCSG1 sample along with the element mapping. It is observed that Zn, Cd, and S are uniformly distributed with strong intensity, suggesting ZCS as the main component. The signal of Mo element is somewhat weak yet it is still evenly distributed within the 1M-ZCSG1 samples indicating successful photodeposition of $MoS_2$ over ZCS and graphene. Furthermore, it is interesting to observe a very thin layer of light contrast substance wrapped over the ZCS nanospheres. This thin substance is not found in the bright-field TEM image, which presumably might be due to its poor contrast, signifying the amorphous structure. The elemental mapping shows that this thin wrapped substance mainly consists of carbon element over the graphene and ZCS nanospheres (Figure 3c). These results justify the proposed schematic fabrication process (Scheme 1) and confirm premediated ZCS–graphene–$MoS_2$ heterostructures, which is consistent with XRD and FESEM results.

XPS analysis was carried out to further investigate the elemental composition and electronic states of elements in the

as-synthesized sample. As depicted in **Figure 4**a, the survey spectrum of the 1M-ZCSG1 sample indicates the presence of Zn, Cd, Mo, S, C, and O elements, signifying high purity of the prepared sample. The sharp XPS peaks at binding energies of 1022 (Zn 2p), 405.6 (Cd 3d), 162.8 (S 2p), 228.8 (Mo 3d), 285 (C 1s), and 532 eV (O 1s) were observed. The O peak can be attributed to the absorption of oxygen on the surface of the sample because of their exposure to the atmosphere. Besides, the XPS spectrum of the 1M-ZCSG1 sample was similar and consistent with the typical ZCS and $MoS_2$ spectrum reported in the literature.[38,53,54] The high-resolution core spectrum of Zn 2p (Figure 4b) illustrates two strong symmetrical spin–orbital peaks at 1022.5 and 1045.6 eV, assigned to Zn $2p_{3/2}$ and Zn $2p_{1/2}$ respectively, allocated to $Zn^{2+}$, which is consistent with the previous results.[16,55–57] Figure 4c displays two strong peaks at 405.4 and 412.1 eV attributed to binding energies of Cd $3d_{5/2}$ and Cd $3d_{3/2}$, respectively, corresponding to $Cd^{2+}$ state.[38,58] The high-resolution XPS spectrum in Figure 4d shows the binding energies of the Mo $3d_{5/2}$ and Mo $3d_{3/2}$ peaks at 228.9 and 232.1 eV, respectively, which are typical values for $Mo^{4+}$ conforming to
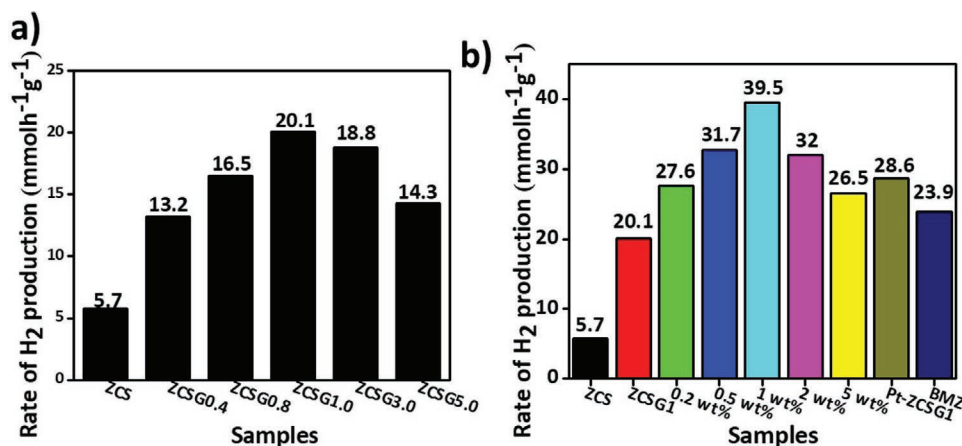
**Figure 5.** Comparison of the photocatalytic hydrogen production activity of a) ZCS samples with different graphene wt%. b) Graphene–ZCS samples with different $MoS_2$ wt% along with Pt doped and $MoS_2$ bulk mixed samples.

$MoS_2$ photodeposition over the surface of the graphene–ZCS composite.[16,38] The characteristic peak for S 2s electrons with the peak at 226.2 eV corresponds to $S^{2-}$ signifying the formation of $MoS_2$ nanostructure. The broad asymmetric curve of S 2p can be deconvoluted into two peaks with binding energies of 161.9 and 162.8 eV, corresponding to S $2p_{3/2}$ and S $2p_{1/2}$, respectively (see Figure 4e). The XPS spectrum of C 1s (Figure 4f) can be fitted with four smaller peaks located at 284.8, 285.7, 287.8, and 289.1 eV, which can be assigned to $sp^2$ bonded carbon (C−O), carbonyl (C=O), and carboxyl (O−C=O) functional groups. Interestingly, the peak at 289.1 eV related to O−C=O has almost disappeared, and the peaks corresponding to C−O and C=O have much lower intensities than those observed in graphene oxide in previous literature.[52,54] This result indicates that the percentage of oxygen-containing functional groups has significantly decreased, and thus, the graphene oxide has been effectively reduced into reduced graphene oxide.[59,60]

Raman spectroscopy is one of the prominent tools for analyzing the structural bonding, crystallinity, and associated defect levels in materials. The Raman spectra of ZCS, ZCSG1, and 1M-ZCSG1 photocatalysts are shown in Figure 4g. The Raman spectrum of pristine ZCS phase showed the most intense band at 308 $cm^{-1}$ and less intense band at 610 $cm^{-1}$ that are assigned to the longitudinal optical phonon (1LO and 2LO), respectively.[61,62] The Raman spectrum of the ZCSG1 sample displays two prominent peaks of graphene at around 1582 and 1352 $cm^{-1}$, which correspond to the well-documented G and D bands, respectively, suggesting that the structure of graphene is maintained in the composites.[63] The G band corresponds to the first-order scattering of the $E_{2g}$ mode observed for $sp^2$ carbon domains, and the D band is associated with structural defects from disordered carbon.[38] The Raman spectrum of reduced graphene oxide is displayed in Figure S6† (Supporting Information). While in the 1M-ZCSG1 sample, $MoS_2$ consists of a major band located at 405 $cm^{-1}$ corresponding to the $A^1_g$ mode (see Figure 4h). The $A^1_g$ corresponds to the vibrations (out-of-plane) of sulfur atoms in opposite directions.[64] Besides, the G band is slightly redshifted to a higher band (1596 $cm^{-1}$), indicating the reduction of GO. Besides, the clear redshift toward the high frequency of G band in comparison with

pristine ZCS and ZCSG1 samples might be due to the spatial confinement of the phonon modes between O-Cd-S and O-Zn-S after combining with graphene and $MoS_2$.[47] The presence of hydroxyl functional groups on graphene acts as the heterogeneous nucleation sites to anchor ZCS nanospheres and growth of a few layers $MoS_2$ on the surface of graphene sheets.[65]

The UV–vis diffused reflectance spectra at ZCS, ZCSG1, and 1M-ZCSG1 samples are shown in Figure S7† (Supporting Information). ZCS nanosphere sample has an adsorption edge at 521 nm and the band gap is estimated to be 2.38 eV by extrapolating the linear plot region of the absorbance squared versus energy, which is in good agreement with the previous reports.[66,67] Compared with the pure ZCS, the graphene and $MoS_2$ clustered ZCS composites exhibited redshift absorbance edges and extended the absorbance to the visible-light region (530–800 nm) due to the presence of graphene in ZCS, which could efficiently enhance the visible-light harvesting capacity.[40] The band-gap energy of the as-prepared ZCS, ZCSG1, and 1M-ZCSG1 nanocomposites has been estimated from the Kumbelka–Munk function versus the photon energy. The estimated band-gap energy of as-prepared ZCS, ZCSG1, and 1G-ZCSG1 samples is 2.38, 2.35, and 2.32 eV, respectively. Furthermore, it is worth to mention that carbon atoms in graphene were not incorporated into the ZCS crystal structure and graphene only acts as a substrate for holding ZCS nanospheres.[68] The color of the $MoS_2$ clustered ZCS–graphene nanosheet photocatalysts changes from bright yellow to yellow-green to black after in situ photodeposition of $MoS_2$ on the surface of ZCS–graphene. These results are consistent with the UV–vis results, which further indicates the strongest visible-light absorbance of 1G-ZCSG1.

The photocatalytic activities of the as-prepared graphene–ZCS composites were evaluated under visible-light irradiation ($\lambda \geq 420$ nm) for their $H_2$-production activities in an aqueous solution of $Na_2S$ and $Na_2SO_3$ as sacrificial agents. As shown in **Figure 5**a, photocatalytic activities were conformed for all graphene–ZCS samples. The pristine ZCS shows 5.7 mmol $h^{-1}$ $g^{-1}$ $H_2$-evolution activity, which is low due to the rapid recombination of photogenerated charge carriers. Meanwhile, the hydrogen evolution activity noticeably increased with the

**ADVANCED
SCIENCE NEWS**

www.advancedsciencenews.com

**ADVANCED
MATERIALS
INTERFACES**

www.advmatinterfaces.de

increasing concentration of the graphene amount in the ZCS hollow nanospheres. Notably, the highest $H_2$-production rate of 20.1 mmol $h^{-1}$ $g^{-1}$ was achieved by doping 1 wt% of graphene content. This value is over 3.5 times higher than that of ZCS. When the graphene content is higher than 1 wt%, it leads to a reduction in the $H_2$-production rate. In particular, when the graphene content is 5 wt% the $H_2$-production rate decreased drastically to 14.3 mmol $h^{-1}$ $g^{-1}$. It is clear that loading more graphene above 1 wt% along with ZCS nanospheres will degrade the photocatalytic $H_2$-production activity. Hence, the optimum graphene content has a significant influence on the photocatalytic activity of the ZCS hollow nanospheres.[69]

The photocatalytic $H_2$-production activity of different amounts of $MoS_2$ coupled photocatalysts is illustrated in Figure 5b. The amount of $MoS_2$ loading was varied from 0 to 5 wt% and it is interesting to know that with increasing $MoS_2$ loading up to an optimum level of 1 wt% the $H_2$ production increased and gradually decreased at higher loading content. Under optimized condition (1 wt%), the rate of $H_2$ production was 39.5 mmol $h^{-1}$ $g^{-1}$, which is 6.9 and 1.9 times significantly higher than the pristine ZCS and ZCSG1, respectively, with an apparent quantum yield (AQY) of 53% at 420 nm visible light. These results illustrate that the active sites of the ultrathin $MoS_2$ nanosheets and superior electrical conductivity of RGO composited ZCS lead to effective separation of the photogenerated charge carriers and thus improve the $H_2$-production activity. A further increase in the loading of $MoS_2$ nanosheets above the optimum level (i.e., >1 wt%) results in the decrease of the $H_2$ evolution rate. This is because excessive $MoS_2$ may shield ZCSG samples from light harvesting and acts as the recombination center for photogenerated electrons and holes. Besides, it should be noted that the photocatalytic $H_2$-production activity of the 1M-ZCSG1 sample is higher than that of 1.0 wt% Pt deposited ZCS (28.6 mmol $h^{-1}$ $g^{-1}$), suggesting our well-designed few-layered $MoS_2$-decorated graphene–ZCS heterojunction can replace transitional noble metal doped catalysts with better performance and lower cost. Further, we made a comprehensive comparison of photocatalytic $H_2$-evolution activities of our optimized 1M-ZCSG1 sample with those of representative ZCS based heterojunction composites reported by other researchers, which is presented in **Figure 6** and Table S2† (Supporting Information). It is significant to note that ultrathin $MoS_2$ modified ZCSG composites always exhibit better activity as compared to bulk $MoS_2$ modified physical mixed ZCS sample, demonstrating the significant advantages of the photodeposition approach of ultrathin $MoS_2$ nanolayers that provide a large number of exposed active sites. Further, it can be seen that our in situ photodeposition of $MoS_2$ over graphene–ZCS heterojunction composite samples exhibits higher $H_2$ evolution activities in comparison with most of the recently reported ZCS-based photocatalysts.[34,38,52,47] Guo et al. had proposed such p-g-n system in which ZCS nanorods were fabricated by the solvothermal method and subsequently incorporated with $MoS_2$ and RGO via dual reduction reaction under UV light.[47] Their proposed p-g-n system showed relatively lower photocatalytic $H_2$-production activity than our results. In addition to the above-published work, the biomolecule-assisted synthesized p-n-g hollow spheres showed very low hydrogen evolution; this might probably due to the defects

induced during the one-pot hydrothermal reaction.[54] It is a well-known fact that the architectural design of photocatalytic systems plays a significant influencing aspect in light harvesting and charge separation. In our system, the hollow ZCS nanospheres with hydrothermally reduced 2D graphene and UV-light-reduced $MoS_2$ nanosheets possess a series of unusual properties, such as efficient light harvesting, immense photoinduced charge separation, outstanding antireflection effect, and high specific surface area. Further, it could be described that the activity of S atoms in the $MoS_2$ molecule is different with respect to their preparation condition and type of semiconductor. Usually, p-type $MoS_2$ with poor electrical conductivity shows no hydrogen evolution reaction activity. However, the nanosized few-layer p-type $MoS_2$ with more exposed edges and unsaturated active S atoms could exhibit a good cocatalytic activity for hydrogen evolution reaction. Graphene with good 2D layered structure and high conductivity could greatly match with layered $MoS_2$ as co-catalyst and rapidly separate and fast transfer photogenerated charge carriers, and thus contribute to the photocatalytic activity of the 1M-ZCSG1 system.

In addition to the photocatalytic hydrogen evolution, another important issue for the practical application of photocatalysts is their stability. The crystal structure and the photocatalytic stabilities were investigated by XRD measurement and the recycling hydrogen evolution reactions, respectively. As shown in Figure S8a† (Supporting Information), there is no obvious difference in the XRD patterns of 1M-ZCSG1 before and after five photoreactions. Figure S8b† (Supporting Information) displays the $H_2$-production curve in cycling photocatalytic runs. After a five-time cycling test, the photocatalytic $H_2$-production activity of 1M-ZCSG1 hollow nanospheres sample showed a little decreased activity. This might be due to the tiny particles of $MoS_2$ nanolayers that might break away from the ZCSG1 catalyst during the long time cycling test; thus, the photocatalytic $H_2$-production activity shows a slight decrease. Moreover, after five cycles of the photocatalytic water splitting reaction no detectable amount of $Cd^{2+}$ was observed in the sacrificial solution. These results demonstrate that 1M-ZCSG1 hollow
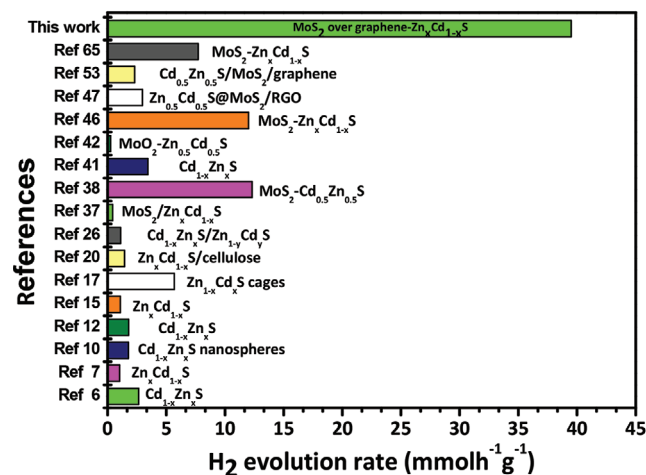


**Figure 6.** Comparison of the photocatalytic hydrogen production activity of 1M-ZCSG1 sample along with previously reported ZCS-based catalysts.
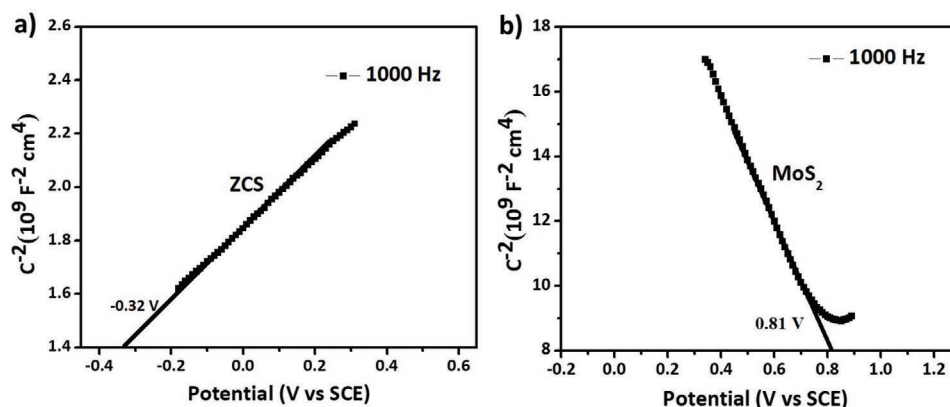
**ADVANCED
SCIENCE NEWS**
www.advancedsciencenews.com

**ADVANCED
MATERIALS
INTERFACES**
www.advmatinterfaces.de

**Figure 7.** Mott–Schottky plots of a) ZCS and b) $MoS_2$ in 0.5 M $Na_2SO_4$ aqueous solution.

nanospheres photocatalyst is relatively stable with remarkable enhanced $H_2$-production activity.

Furthermore, the Mott–Schottky (M-S) analysis was employed to determine both donor density and semiconductor type at semiconductor/liquid interface. It is well known that the type of semiconductor can be determined from the slope of the M-S plot.[70] The positive slope of M-S plot in **Figure 7**a clearly indicates the n-type semiconductor properties of ZCS with electrons as the majority charge carriers. On the contrary, the M-S curve of $MoS_2$, shown in Figure 7b, has a negative slope, confirming that it is a p-type semiconductor with low charge carrier density.[71] The estimated conduction band ($E_{CB}$) values of ZCS and $MoS_2$ samples were –0.32 V and 0.81 V versus saturated calomel electrode, respectively, which implies that the CB edge potential at normal hydrogen electrode of ZCS is more negative than that of $MoS_2$. Further, by considering UV–vis diffuse reflectance spectra (DRS) absorption results, the valence band potential ($E_{VB}$) of ZCS and $MoS_2$ is calculated using the $E_{VB} = E_{CB} + E_g$ equation.[72,73] From the DRS results the $E_{VB}$ is calculated to be 2.04 and 1.4 V, respectively. Further the value of the $E_g$ for ZCS and $MoS_2$ is determined to be 2.36 and 2.21 eV, respectively.

The band structure alignment and the resulting charge separation of the ZCS and $RGO/MoS_2$ composite are shown in **Scheme 2**. The Fermi levels of the p-type $MoS_2$ and n-type $MoS_2$ semiconductors align at equilibrium to form p-n junction, and the internal electric field across the interface is produced. Under visible-light illumination both semiconductors could be excited and produce photogenerated electrons and holes. Before connection p-type $MoS_2$ and n-type ZCS semiconductors normally have different positions of Fermi levels. After connection, because of higher Fermi level of ZCS a readjustment of the Fermi level takes place, and the CB bottom of $MoS_2$ becomes higher than that of ZCS. Under visible-light illumination, the electrons in VB of $MoS_2$ will be excited to CB, leaving holes in VB. The photogenerated electrons on $MoS_2$ transfer easily to RGO and ZCS because of lower CB position than that of $MoS_2$. Thus, the electron-hole pair separation is greatly improved by the development of p-n junction and resulting in enhanced hydrogen evolution. Besides, some of the photogenerated electrons of the ZCS and the electrons that migrated from the $MoS_2$ nanosheets to ZCS could

be attracted by highly conducting graphene nanosheets and thus reduce the charge recombination by forming numerous p-g-n junctions to further enhance the charge separation. The photogenerated holes accumulated at the $MoS_2$ can be consumed by the $Na_2S$-$Na_2SO_3$ sacrificial reagent solution, thus enhancing $H_2$ generation.

A series of photoluminescence (PL) experiments were conducted to understand photogenerated electron–hole pair
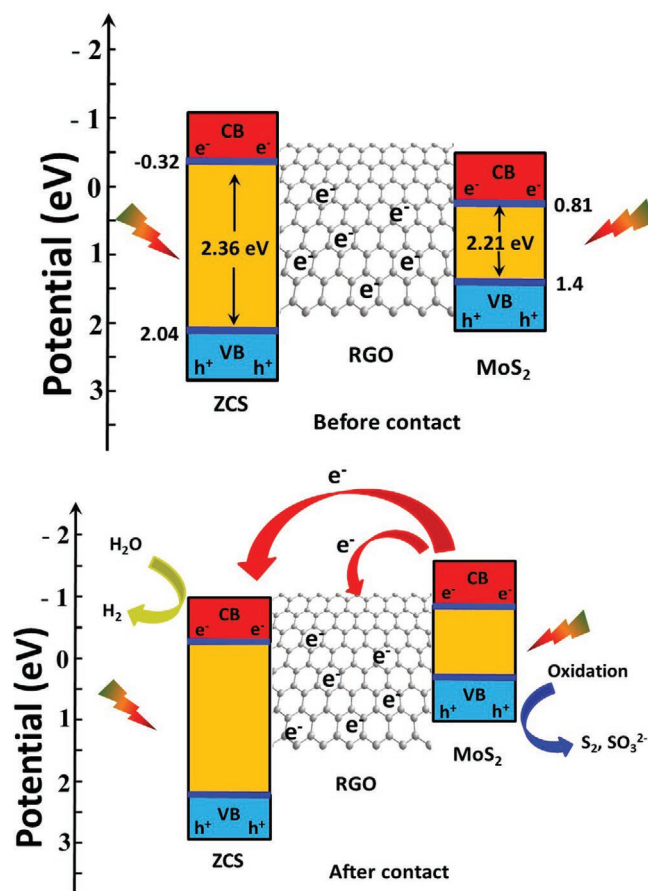


**Scheme 2.** Schematic illustration of the charge-transfer process for photocatalytic $H_2$ evolution in 1M-ZCSG1 nanoheterojunctions.
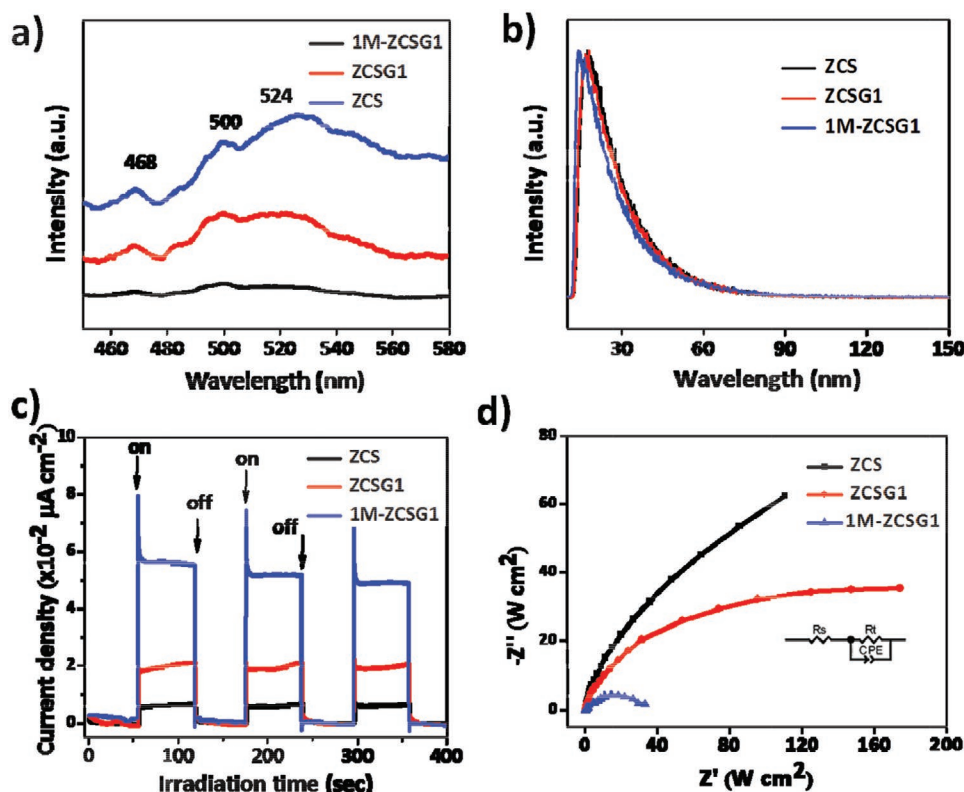
**2000010** (8 of 13)

**Figure 8.** a) Static photoluminescence curves (*Ex* = 390 nm). b) Photoluminescence decay curves. c) Transient photocurrent. d) Electrochemical impedance spectroscopy of as-prepared ZCS, ZCSG1, and 1M-ZCSG1.

separation and electron transfer performance between ZCS, ZCSG1, and 1M-ZCSG1 samples. It is well known that the intensity of PL spectra depends upon the recombination rate of photogenerated excitons. Furthermore, it has been observed that the higher the recombination rate of electron/hole pairs, the higher the PL emission.[74–76] The result in **Figure 8**a indicates that the ZCS sample shows strong emission peaks in the range of 430–500 nm and a weak emission at 524 nm. The emission peak at 500 nm is due to the recombination of electrons from the energy level of sulfur vacancies of metal chalcogenides, which is consistent with the previous reports.[77] The weak emission of cadmium sulfide luminescence is observed at 524 nm.[78] It is observed that the sharpness of the peak falls with the loading of MoS$_2$ over the ZCSG1 sample suggesting that the addition of MoS$_2$ nanosheets significantly inhibits the recombination of electron–hole pairs and enhances the photocatalytic activity. Time-resolved photoluminescence spectroscopic analysis was performed to further get an insight into the charge-transfer process between ZCS, ZCSG1, and 1M-ZCSG1 hollow nanostructures. The samples were excited at a wavelength at 375 nm and the emission obtained at 500 nm is shown in Figure 8b. PL decay profiles are fitted with biexponential function to calculate the exciton lifetime, $\langle \tau \rangle$. As compared with the ZCS sample, the shorter lifetime and longer lifetime of 1G-ZCSG1 decreased from 0.39 to 0.15 ns and from 8.43 to 5.27 ns. The shorter lifetime is due to the decay from free exciton states while the longer lifetime is from the bound exciton states.[79–81] The decreased lifetime indicates

more nonradiative transitions existing in 1M-ZCSG1, which is induced by the easier exciton transfer from MoS$_2$ to surface due to the shorter pathway caused by uniform dispersion over ZCS–graphene hollow nanospheres. These results clearly illustrate that the shorter emission lifetime and smaller interfacial electron-transfer resistance are achieved in the 1M-ZCSG1 nanocomposite sample, which is beneficial for enhanced photocatalytic H$_2$-evolution activity.[82,83]

The transient photocurrent result of as-prepared ZCS, ZCSG1, and 1M-ZCSG1 samples was recorded via several on–off cycles at the periodic 400 nm LED-light irradiation at a bias potential of 0.5 V. The photocurrent–time (*I–t*) curves of the above-mentioned samples are illustrated in Figure 8c. As shown, the ZCS sample demonstrates a clear photocurrent response and their value rapidly increased as soon as the light turned on, and the value decreased to zero when the light turned off. This result also indicates that the photogenerated electrons and holes are efficiently transferred at the sample/electrode interface to produce photocurrent under visible-light illumination.[84] It can be seen that pure ZCS exhibits low photocurrent density, which can be attributed to the fast recombination of photogenerated electrons and holes. Notably, 1M-ZCSG1 samples show the highest photocurrent intensity among the three samples. This observation indicates that p-g-n hierarchical heterostructures allow more efficient separation of photogenerated electron–hole pairs as compared to the ZCS and ZCSG1 samples. Therefore, it can be concluded that the higher photocurrent intensity indicates a higher efficiency

**ADVANCED
SCIENCE NEWS**

www.advancedsciencenews.com

**ADVANCED
MATERIALS
INTERFACES**

www.advmatinterfaces.de

in the separation of the photoexcited electron–hole pairs and enhanced diffusion of the charges, which are favorable for the enhanced photocatalytic activity.

Electrochemical impedance spectroscopy (EIS) experiments were performed to understand the charge-transfer kinetics process occurring in the three-electrode system. The semicircle in the plot is attributed to the charge-transfer resistance $R_t$ in parallel with the double-layer capacitance, and the EIS Nyquist plot can be simulated by an electrical equivalent circuit model.[85] In the model $R_s$ is the total ohmic resistance of the electrolyte solution.[86] Figure 8d displays the EIS Nyquist plots of ZCS, ZCSG1, and 1M-ZCSG1 heterojunctions. The 1M-ZCSG1 nanostructure exhibits the smallest semicircle among the three samples, indicating the lowest charge transfer resistance, and thus facilitates higher separation and transfer rate of electron–hole pairs.[87–89] This result is consistent with the transient photocurrent responses and PL results confirming the 1M-ZCSG1 sample as the optimum sample for photocatalytic hydrogen evolution.

According to the above photocatalytic experimental results, it could be concluded that the enhanced $H_2$-evolution of 1M-ZCSG1 nanocomposite sample can be attributed to the collective outcome of several factors. First, ZCS with hollow nanostructure could assist in the easy transportation of reactants and products on the photocatalyst surfaces and result in easy chemical reactions.[53] Second, the hollow nanospheres assembled by tiny particles on the surfaces could allow multiple reflections of light, thus enhancing light harvesting and increasing the photogenerated charge carriers.[51] Third, the uniformly decorated ZCS nanospheres on the graphene sheets, with close contact between graphene and $MoS_2$ sheets, could promote the efficient charge transfer between graphene/$MoS_2$ and ZCS. Finally, the heterojunctions between p-type $MoS_2$ nanosheets and n-type ZCS hollow nanospheres could effectively separate photogenerated electrons and holes and enhance the $H_2$-production activity.

## 3. Conclusions

In summary, few layers of $MoS_2$ nanosheets were successfully incorporated onto graphene composited ZCS hollow nanospheres via hydrothermal method followed by in situ photodeposition. The $MoS_2$ nanosheets are deposited on the surface of ZCS hollow nanospheres with graphene sheets to form intimate contact interfaces. The highest $H_2$-production rate of 39.5 mmol h$^{-1}$ g$^{-1}$ was achieved by depositing 1 wt % of $MoS_2$ over the 1M-ZCSG1 sample, which is 6.9 and 1.9 times significantly higher than the pristine ZCS and 1 wt % graphene composited ZCS samples, respectively, with an AQY of 53% at 420 nm visible light. The as-prepared 1M-ZCSG1 hollow nanospheres photocatalyst is relatively stable with remarkable enhanced $H_2$-production activity. The possible mechanism for significantly enhanced hydrogen evolution is proposed to explain observed $H_2$ evolution activity enhancement in the $MoS_2$ coupled graphene composited ZCS sample, which was further confirmed by photoluminescence and time-resolved photoluminescence characterizations. The enhanced performance of $H_2$ evolution in the 1M-ZCSG1 sample is attributed

to the 2D structure of $MoS_2$ and graphene, allowing efficient transfer of the photoexcited electron to the reactant. The interface between ZCS, 2D graphene, and $MoS_2$ nanosheets, forming p-g-n heterojunction, enables fast electron transfer from the conduction band of ZCS to the graphene and $MoS_2$ nanosheets, further suppressing the electron–hole recombination that was confirmed by electrochemical impedance spectroscopy. The current study sheds new light on advancing the higher performance and noble-metal-free photocatalysts for $H_2$ production under visible-light irradiation by combining 2D materials with traditional nanophotocatalysts.

## 4. Experimental Section

*Preparation of Zn$_{0.5}$Cd$_{0.5}$S Nanospheres*: All the chemical reagents used in this study were of analytical grade (purchased from Shanghai Chemical Reagent Co., China) and used as received. Distilled water was used in all experiments. In a typical synthesis, zinc acetate (1.8 mmol) and cadmium acetate (1.8 mmol) were dissolved in 120 mL distilled water with magnetic stirring at room temperature for 30 min to obtain a uniform solution. After that, thiourea (90 mmol) was added to the solution, which was stirred for another 30 min and then transferred to a 180 mL Teflon-lined stainless steel autoclave. The autoclave was maintained at 150 °C for 5 h for the hydrothermal reaction. After the mixture was cooled naturally to room temperature, the yellow precipitates were centrifuged, washed with ethanol and distilled water five times, rinsed with carbon disulfide, and then dried in an oven at 60 °C for 8 h.

*Synthesis of Graphene–Zn$_{0.5}$Cd$_{0.5}$S Nanoheterojunction*: GO was synthesized from natural graphite powder (>99.8%, Alfa Aesar) via a modified Hummer's method. Graphene–ZCS nanospheres were prepared by a simple hydrothermal method using ethanol–water as a solvent. In a typical synthesis, a certain amount of GO was dispersed in a mixed solution of distilled water (20 mL) and ethanol (10 mL) by ultrasonic treatment for 1 h, and then 0.2 g of as-prepared ZCS nanospheres was added to the obtained GO solution and stirred for another 1 h to obtain a homogeneous suspension. The resultant mixture was transferred into a 50 mL Teflon-lined stainless autoclave and heated at 180 °C for 3 h under autogenously pressure to simultaneously achieve the reduction of GO and the deposition of ZCS catalyst on the graphene substrate. After the reaction, the reacted mixture was collected, washed with distilled water and ethanol, and then dried in an oven at 80 °C for 8 h. To investigate the effect of graphene on the photocatalytic hydrogen evolution under visible light, the weight percentage of graphene to Zn$_{0.5}$Cd$_{0.5}$S catalyst was varied from 0.4 to 5 (0.4, 0.8, 1.0, 3.0, and 5.0 wt%), and the corresponding samples were labeled as graphene–Zn$_{0.5}$Cd$_{0.5}$S (ZCSGX) where X = 0.4, 0.8, 1.0, 3.0, and 5.0 wt%, respectively.

*Synthesis of XM-ZCSG1 Nanoheterojunction*: $MoS_2$ was synthesized according to the previous literature.[37] In situ photodeposition of $MoS_2$ was carried out at room temperature in a closed system. Briefly, 80 mL aqueous solution of Na$_2$S (0.35 M) and Na$_2$SO$_3$ (0.25 M) in a gas-tight closed three-neck Pyrex flask was well degassed by nitrogen gas for 1 h to remove dissolved oxygen. 10 mg of graphene–ZCS nanospheres and a predetermined volume of (NH4)$_2$MoS$_4$ precursor solution were added. Before illumination, the reaction mixture was vigorously stirred and further degassed by nitrogen gas for 30 min. The reaction mixture was then irradiated by a 300 W Xe lamp for 1 h. The resulting precipitate was collected, washed thoroughly with distilled water followed by washing in ethanol, and then dried in an oven at 80 °C for 8 h. To further investigate the effect of the content of the $MoS_2$ co-catalyst on the photocatalytic hydrogen evolution activity of graphene–ZCS nanospheres, a series of composites were prepared by varying the amount of $MoS_2$ loading and the corresponding samples were labeled as XM-ZCSG1 where X = 0.2, 0.5, 1.0, 2.0, and 5.0 wt%. For

comparison, platinum was deposited onto the ZCSG1 sample through the photodeposition method. The typical preparation condition was as follows: 0.2 g of ZCSG1 sample was dispersed in a 50 mL of water and 1 wt % of $H_2PtCl_6.6H_2O$ was dropped under stirring for 30 min. Then, the above suspension was stirred and irradiated by a 300 W Xe lamp. After irradiation for 30 min, the sample was washed with distilled water and collected by centrifugation and dried at 80 °C overnight. The obtained sample was denoted as Pt-ZCSG1. Furthermore, 1 wt % of commercial bulk $MoS_2$ power (Aladdin Reagent Company) was composited with the ZCSG1 sample and the corresponding sample was denoted as BMZ.

*Characterization*: The powder XRD patterns of as-prepared samples were obtained on an X-ray diffractometer (type HZG41B-PC) using monochromatized Cu K$\alpha$ (0.15418 nm) at a scan rate (2$\theta$) of 0.05° s$^{-1}$. The accelerating voltage and applied current were 40 kV and 80 mA, respectively. FESEM (ZEISS, Gemini SEM 450 Germany) images were recorded at an accelerating voltage of 5 kV and equipped with EDS. TEM and HRTEM analyses were conducted using Tecnai G2 20 U-Twin electron microscope operating at 200 kV. The BET specific surface area ($S_{BET}$) of the powders was analyzed by nitrogen adsorption in a Micromeritics ASAP 2020 nitrogen adsorption apparatus (USA). All the as-prepared samples were degassed at 180 °C before nitrogen adsorption measurements. The BET surface area was determined by a multipoint BET method using the adsorption data in the relative pressure ($P/P_0$) range of 0.05–0.3. A desorption isotherm was used to determine the pore-size distribution via the BJH method, assuming a cylindrical pore model.[90] The nitrogen adsorption volume at the relative pressure ($P/P_0$) of 0.994 was used to determine the pore volume and average pore size. AFM images were obtained using (Asylum Research, MFP-3D Stand-Alone). The surface morphology of the sample was acquired in tapping mode. The samples were prepared by dropping the reaction solution onto a silicon wafer substrate followed by drying at room temperature. Raman spectra were recorded at room temperature with a micro-Raman spectrometer (Horiba Scientific) in the backscattering geometry with a 512 nm and Ar$^+$ laser as an excitation source. The XPS measurement was performed in an ultrahigh vacuum VG ESCALAB 210 electron spectrometer using Mg K$\alpha$ (1253.6 eV) radiation source (operating at 200 W) of a twin anode in the constant analyzer energy mode with a pass energy of 30 eV. All the binding energies were referenced to the adventitious C 1s line at 284.8 eV as the internal standard. UV–vis absorbance spectra of composite powders were obtained for the dry-pressed disk samples with a UV–vis spectrophotometer (UV-2550, Shimadzu, Japan) using $BaSO_4$ as a standard. The photoluminescence emission lifetimes of the samples were obtained by time-resolved transient PL spectroscopy (FLS920 Edinburgh Instrument, UK).

*Photocatalytic Hydrogen Production*: The photocatalytic hydrogen production experiments were performed in 100 mL Pyrex flask at ambient temperature and atmospheric pressure, and openings of the flask were sealed with a silicone rubber septum. A 300 W Xe arc lamp through a UV-cutoff filter (≤420 nm) positioned 5 cm in front of the photocatalytic reactor was used as a visible-light source (22 cm far away from the photocatalytic reactor). The focused intensity on the flask measured by a visible-light radiometer (Model: FZ-A, China) was ≈150 mW cm$^{-2}$ in the wavelength range of 420–1000 nm. In typical photocatalytic experiments, 10 mg of catalyst was suspended in 80 mL mixed aqueous solution containing 0.35 M $Na_2S$ and 0.25 M $Na_2SO_3$. Before irradiation, the suspensions were bubbled by nitrogen for 30 min to remove the dissolved oxygen and to ensure that the reaction system was under anaerobic conditions. A continuous magnetic stirrer was applied at the bottom of the reactor to keep the photocatalyst particles in a suspension state during the whole experiment. 0.4 mL of gas was intermittently sampled through the septum, and hydrogen concentration was analyzed by gas chromatography (GC–14C, Shimadzu, Japan, TCD, nitrogen as a carrier gas and 5 Å molecular sieve column). All glassware was carefully rinsed with distilled water before use. The AQY was also measured under the same photocatalytic reaction conditions except that

the light source was different. Four LEDs (3 W, 420 nm, Shenzhen LAM-PLIC Science Co. Ltd., China), positioned 1 cm away from the reactor in four different directions, were used as light sources to trigger the photocatalytic reaction. The focused intensity and areas on the flask for each were ≈6.0 mW cm$^{-2}$ and 1 cm$^2$, respectively. The AQY was calculated according to Equation (1)

$$AQY[\%] = \frac{\text{number of reacted electrons}}{\text{number of incident photons}} \times 100 \qquad (1)$$

$$= \frac{\text{number of evolved } H_2 \text{ molecules} \times 2}{\text{number of incident photons}} \times 100$$

*Photoelectrochemical Measurements*: Photocurrents were measured by an electrochemical analyzer (CHI660C Instruments, CHI, China) in a standard three-electrode system using the prepared samples as the working electrodes with an active area of ≈0.5 cm$^2$, a Pt wire as the counter electrode, and Ag/AgCl (saturates KCl) as a reference electrode. Four LEDs (3 W, 420 nm, Shenzhen LAM-PLIC Science Co. Ltd., China), positioned 1 cm away from the reactor, were used as visible-light sources. The photoanode was kept at a 15 cm distance from the light source. The integrated visible-light intensity measured with a visible-light radiometer (FZ-A) was 20 mW cm$^{-2}$. A 0.5 M $Na_2SO_4$ aqueous solution was used as the electrolyte. Working electrodes were prepared as follows: 0.05 g of photocatalyst (samples ZCS, ZCSG1, and 1M-ZCSG1) was ground with 0.02 g of polyethylene glycol (molecular weight: 20 000) and 0.5 mL of ethanol to make a slurry. The slurry was then coated onto a 2 cm × 1.2 cm F-doped SnO$_2$ coated glass (FTO glass) electrode by the doctor blade technique. Next, these electrodes were dried in a tubular furnace in a nitrogen atmosphere at 500 °C for 30 min. All investigated electrodes had a similar film thickness of 10–11 μm. The band structures of ZCS and $MoS_2$ catalysts were measured in 0.5 M $Na_2SO_4$ aqueous solution at 1000 Hz frequency on an electrochemical workstation (CHI660C Instrument).

## Supporting Information

Supporting Information is available from the Wiley Online Library or from the author.

## Acknowledgements

ADVANCED
MATERIALS
INTERFACES
www.advmatinterfaces.de

21967350, 2020, 12, Downloaded from https://onlinelibrary.wiley.com/doi/10.1002/admi.202000010 by Hanyang University Library, Wiley Online Library on [09/10/2023]. See the Terms and Conditions (https://onlinelibrary.wiley.com/terms-and-conditions) on Wiley Online Library for rules of use; OA articles are governed by the applicable Creative Commons License

## Conflict of Interest

The authors declare no conflict of interest.

## Keywords

[1] W. J. Zhang, Y. Hu, L. B. Ma, G. Y. Zhu, Y. R. Wang, X. L. Xue, R. P. Chen, S. Y. Yang, Z. Jin, *Adv. Sci.* **2018**, *5*, 1700275.

[2] X. B. Chen, S. H. Shen, L. J. Guo, S. S. Mao, *Chem. Rev.* **2010**, *110*, 6503.

[3] A. Kudo, Y. Miseki, *Chem. Soc. Rev.* **2009**, *38*, 253.

[4] J. K. Stolarczyk, B. Santanu, P. Lakshminarayana, J. Feidmann, *ACS Catal.* **2018**, *8*, 3602.

[5] J. G. Song, H. T. Zhao, R. R. Sun, X. Y. Li, D. J. Sun, *Energy Environ. Sci.* **2017**, *10*, 225.

[6] L. Wang, W. Z. Wang, M. Shang, W. Z. Yin, S. M. Sun, L. Zhang, *Int. J. Hydrogen Energy* **2010**, *35*, 19.

[7] C. C. Chan, C. C. Chang, C. H. Hsu, Y. C. Weng, K. Y. Chen, H. H. Lin, W. C. Huang, S. F. Cheng, *Int. J. Hydrogen Energy* **2014**, *39*, 1630.

[8] M. C. Liu, D. W. Jing, Z. H. Zhou, L. J. Guo, *Nat. Commun.* **2013**, *4*, 2278.

[9] X. Z. Yue, S. Yi, R. W. Wang, Z. T. Zhang, S. L. Qiu, *Appl. Catal., B* **2018**, *224*, 17.

[10] H. Y. Zhou, Q. Y. Liu, W. M. Liu, J. C. Ge, M. Lan, C. Wang, J. X. Geng, P. F. Wang, *Chem. - Asian J.* **2014**, *9*, 811.

[11] P. A. L. Lopes, A. J. S. Mascarenhas, L. A. Silva, *J. Alloys Compd.* **2015**, *649*, 332.

[12] M. C. Liu, L. Z. Wang, G. Q. Lu, X. D. Yao, L. J. Guo, *Energy Environ. Sci.* **2011**, *4*, 1372.

[13] Z. W. Mei, B. K. Zhang, J. X. Zheng, S. Yuan, Z. Q. Zhuo, X. G. Meng, Z. G. Chen, K. Amine, W. L. Yang, L. W. Wang, W. Wang, S. F. Wang, Q. H. Gong, J. Li, F. S. Liu, F. Pan, *Nano Energy* **2016**, *26*, 405.

[14] Y. G. Cheng, S. Zhao, X. Wang, Q. Peng, R. Lin, Y. Wang, R. A. Shen, X. Cao, L. B. Zhang, G. Zhou, J. Li, A. D. Xia, Y. D. Li, *J. Am. Chem. Soc.* **2016**, *138*, 4286.

[15] Y. Wang, J. C. Wu, J. W. Zheng, R. Xu, *Catal. Sci. Technol.* **2011**, *1*, 940.

[16] Y. J. Hao, S. Z. Kang, X. Liu, X. Q. Li, L. X. Qin, J. Mu, *ACS Sustainable Chem. Eng.* **2017**, *5*, 1165.

[17] J. M. Chen, J. Y. Chen, Y. W. Li, *J. Mater. Chem. A* **2017**, *5*, 24116.

[18] X. H. Zhang, D. W. Jing, M. C. Liu, L. Guo, *Catal. Commun.* **2008**, *9*, 1720.

[19] Y. Liu, G. R. Wang, Y. L. Ma, Z. L. Jin, *Catal. Lett.* **2019**, *149*, 1788.

[20] P. P. Wang, Z. B. Geng, J. X. Gao, R. F. Xuan, P. Liu, Y. Wang, K. Huang, Y. Wan, Y. Xu, *J. Mater. Chem. A* **2015**, *3*, 1709.

[21] X. X. Zhao, J. Feng, J. Liu, W. Shi, G. M. Yang, G. C. Wang, P. Cheng, *Angew. Chem., Int. Ed.* **2018**, *57*, 9790.

[22] H. Du, K. Liang, C. Z. Yuan, H. L. Gou, X. Zhou, Y. F. Jiang, A. W. Xu, *ACS Appl. Mater. Interfaces* **2016**, *8*, 24550.

[23] C. Zeng, Y. Hu, T. Zhang, F. Dong, Y. Zhang, H. W. Huang, *J. Mater. Chem. A* **2018**, *6*, 16932.

[24] X. Wang, J. Chen, X. J. Guan, L. Guo, *Int. J. Hydrogen Energy* **2015**, *40*, 7546.

[25] K. Li, R. Chen, L. S. Li, S. L. Xie, L. Z. Dong, Z. H. Kang, J. C. Bao, Y. Q. Lan, *ACS Appl. Mater. Interfaces* **2016**, *8*, 14535.

[26] X. W. Wang, W. Y. Wang, B. Du, C. X. Zhou, G. Feng, J. X. Cai, T. Wang, R. B. Zhang, *J. Alloys Compd.* **2017**, *705*, 683.

[27] M. C. Liu, Y. B. Chen, J. Z. Su, J. W. Shi, X. Wang, K. J. Guo, *Nat. Energy* **2016**, *1*, 16151.

[28] M. Fayette, R. D. Robinson, *J. Mater. Chem. A* **2014**, *2*, 5965.

[29] L. Wang, Z. P. Yao, H. Z. Jia, B. Chen, Z. H. Jiang, *Dalton Trans.* **2013**, *42*, 9976.

[30] Z. Han, G. Chen, C. Li, Y. G. Yu, Y. X. Zhou, *J. Mater. Chem. A* **2015**, *3*, 1696.

[31] Q. J. Xiang, J. G. Yu, M. Jaroniec, *Chem. Soc. Rev.* **2012**, *41*, 782.

[32] Q. C. Yuan, D. Liu, N. Zhang, W. Ye, H. X. Ju, L. Shi, R. Long, J. F. Zhu, Y. J. Xiong, *Angew. Chem., Int. Ed.* **2017**, *56*, 4206.

[33] Q. Li, H. Meng, J. G. Yu, W. Xiao, Y. Q. Zheng, J. Wang, *Chem. - Eur. J.* **2014**, *20*, 1176.

[34] D. Voiry, R. Fullon, J. Yang, C. C. C. Silva, K. Rajesh, I. Bozkurt, D. Kaplan, M. J. Lagos, P. E. Batson, G. Gautam, D. M. Aditya, L. Er, D. Dong, V. B. Shenoy, T. Asefa, C. Manish, *Nat. Mater.* **2016**, *15*, 1003.

[35] K. Chang, M. Li, T. Wang, S. X. Ouyang, P. Li, L. Q. Liu, J. H. Ye, *Adv. Energy Mater.* **2015**, *5*, 1402279.

[36] D. Voiry, J. Yang, C. Manish, *Adv. Mater.* **2016**, *28*, 6197.

[37] M. Nguyen, P. D. Tran, S. S. Pramana, L. L. Lee, S. K. Batabyal, N. Mathews, L. H. Wong, M. Graetzel, *Nanoscale* **2013**, *5*, 1479.

[38] S. J. Zhao, J. J. Huang, Q. Y. Huo, X. Z. Zhou, W. X. Tu, *J. Mater. Chem. A* **2016**, *4*, 193.

[39] W. Zhang, R. Xu, *Int. J. Hydrogen Energy* **2009**, *34*, 8495.

[40] J. Zhang, L. F. Qi, J. R. Ran, J. G. Yu, S. Z. Qiao, *Adv. Energy Mater.* **2014**, *4*, 1310925.

[41] Y. Zhou, Y. G. Wang, T. Wen, S. Zhang, B. B. Chang, Y. Z. Guo, B. C. Yang, *J. Colloid Interface Sci.* **2016**, *467*, 97.

[42] H. Du, X. Xie, Q. Zhu, L. Lin, Y. F. Jiang, Z. K. Yang, X. Zhou, A. W. Xu, *Nanoscale* **2015**, *7*, 5752.

[43] Y. Wang, J. C. Wu, J. W. Zheng, R. Jiang, R. Xu, *Catal. Sci. Technol.* **2012**, *2*, 581.

[44] D. S. Dia, L. Wang, N. Xiao, S. S. Li, H. Xu, S. Liu, B. Xu, D. Lv, Y. Q. Gao, W. Song, L. GeJ. Liu, *Appl. Catal., B* **2018**, *233*, 194.

[45] J. R. Ran, J. Zhang, J. G. Yu, S. Z. Qiao, *ChemSusChem* **2014**, *7*, 3426.

[46] R. Gholipour, C. C. Nguyen, F. Béland, T. O. Do, *J. Photochem. Photobiol., A* **2018**, *358*, 1.

[47] S. N. Guo, Y. L. Min, J. C. Fan, Q. Xu, *ACS Appl. Mater. Interfaces* **2016**, *8*, 2928.

[48] W. C. Wang, S. Zhu, Y. N. Cao, Y. Tao, X. Li, D. L. Pan, D. L. Phillips, D. Q. Zhang, M. Chen, G. S. Li, H. X. Li, *Adv. Funct. Mater.* **2019**, *29*, 1901958.

[49] L. Xu, Q. Q. Jiang, Z. H. Xiao, X. Y. Li, J. Huo, S. Y. Wang, L. M. Dia, *Angew. Chem., Int. Ed.* **2016**, *55*, 5277.

[50] A. A. S. Goncalves, M. Jaroniec, *J. Colloid Interface Sci.* **2019**, *537*, 725.

[51] H. L. Xiong, L. L. Wu, Y. Liu, T. N. Gao, K. Q. Li, Y. Long, R. Zhang, L. Zhang, Z. A. Qiao, Q. S. Huo, X. Ge, S. Y. Song, H. J. Zhang, *Adv. Energy Mater.* **2019**, *9*, 1901634.

[52] P. Madhusudan, J. G. Yu, W. W. Wang, B. Cheng, G. Liu, *Dalton Trans.* **2012**, *41*, 14345.

[53] R. F. Du, Y. Zhang, B. Y. Li, X. L. Yu, H. J. Liu, X. Q. An, J. H. Qu, *Phys. Chem. Chem. Phys.* **2016**, *18*, 16208.

[54] Y. B. Chen, L. J. Guo, *J. Mater. Chem.* **2012**, *22*, 7507.

[55] A. Hezam, K. Namratha, Q. A. Drmosh, B. N. Chandrashekar, K. K. Sadasivuni, Z. H. Yamani, C. Cheng, K. Byrappa, *CrystEngComm* **2017**, *19*, 3299.

[56] P. Madhusudan, Y. Wang, B. N. Chandrashekar, W. J. Wang, J. W. Wang, J. Miao, R. Shi, Y. X. Liang, G. J. Mi, C. Cheng, *Appl. Catal., B* **2019**, *253*, 379.

[57] P. F. Wang, S. Zhan, H. T. Wang, Y. G. Xia, Q. L. Hou, Q. X. Zhou, Y. Li, K. R. Rajesh, *Appl. Catal., B* **2018**, *230*, 210.

[58] F. X. Xiao, J. W. Miao, B. Liu, *J. Am. Chem. Soc.* **2014**, *136*, 1559.

[59] S. P. Sasikala, P. Poulin, C. Aymonier, *Adv. Mater.* **2017**, *29*, 1605473.

[60] J. Su, G. D. Li, X. H. Li, J. S. Chen, *Adv. Sci.* **2019**, *6*, 1801702.

[61] M. Ichimura, T. Furukawa, K. Shirai, T. Goto, *Mater. Lett.* **1997**, *33*, 51.

[62] V. K. Prashant, *J. Phys. Chem. Lett.* **2010**, *1*, 520.

[63] Y. Li, Z. W. Li, C. Chi, H. Y. Shan, L. H. Zheng, Z. Y. Fang, *Adv. Sci.* **2017**, *4*, 1600430.

[64] N. Jeong, H. K. Kim, W. S. Kim, J. Y. Choi, J. H. Han, J. Y. Nam, K. S. Hwang, S. C. Yang, E. J. Jwa, T. Y. Kim, S. C. Park, Y. S. Seo, S. I. Kim, *Chem. Eng. J.* **2019**, *356*, 292.

[65] Y. T. Lu, D. D. Wang, P. Yang, Y. Du, C. Lu, *Catal. Sci. Technol.* **2014**, *4*, 2650.

[66] Q. Li, B. Guo, J. G. Yu, J. R. Ran, B. H. Zhang, H. J. Yan, J. R. Gong, *J. Am. Chem. Soc.* **2011**, *133*, 10878.

[67] X. L. Zhu, S. Yu, X. Z. Gong, C. Xue, *ChemPlusChem* **2018**, *83*, 825.

[68] J. Zhang, J. G. Yu, M. Jaroniec, J. G. Gong, *Nano Lett.* **2012**, *12*, 4584.

[69] P. Madhusudan, S. Wageh, A. A. Al-Ghamdi, J. Zhang, B. Cheng, Y. Yu, *Appl. Surf. Sci.* **2020**, *506*, 144683.

[70] Y. Liu, H. T. Niu, W. Gu, X. Y. Cai, B. D. Mao, D. Li, W. D. Shi, *Chem. Eng. J.* **2018**, *339*, 117.

[71] Z. X. Zheng, Y. Qiao, Y. Cai, Y. He, Y. M. Tang, L. S. Li, *J. Colloid Interface Sci.* **2019**, *533*, 561.

[72] P. Madhusudan, J. R. Ran, J. Zhang, J. G. Yu, G. Liu, *Appl. Catal., B* **2011**, *110*, 286.

[73] X. X. Han, S. Heuser, X. Tong, N. J. Yang, X. Y. Guo, X. Jiang, *Chem. - Eur. J.* **2020**, *26*, 3590.

[74] C. Cheng, A. Amini, C. Zhu, Z. Xu, H. S. Song, N. Wang, *Sci. Rep.* **2015**, *4*, 4181.

[75] S. Wang, Y. Wang, S. L. Zhang, S. Q. Zang, X. W. Lou, *Adv. Mater.* **2019**, *31*, 1903404.

[76] Y. G. Chao, P. Zhou, N. Li, J. P. Lai, Y. Yang, Y. L. Zhang, Y. G. Tang, W. X. Yang, Y. P. Du, D. Su, Y. S. Tan, S. J. Guo, *Adv. Mater.* **2019**, *31*, 1807226.

[77] S. K. Apte, S. N. Garaje, G. P. Mane, A. Vinu, S. D. Naik, D. P. Amalnerkar, B. B. Kale, *Small* **2011**, *7*, 957.

[78] Z. Zhang, J. Huang, M. Zhang, Q. Yuan, B. Dong, *Appl. Catal., B* **2015**, *163*, 298.

[79] S. S. Kai, B. J. Xi, Y. F. Wang, S. L. Xiong, *Chem. - Eur. J.* **2017**, *23*, 16653.

[80] R. Marschall, *Adv. Funct. Mater.* **2014**, *24*, 2421.

[81] H. N. Shi, S. R. Long, J. G. Hou, L. Ye, Y. W. Sun, W. J. Ni, C. S. Song, K. Y. Li, G. G. Gurzadyan, X. W. Guo, *Chem. - Eur. J.* **2019**, *25*, 5028.

[82] Y. C. Wang, J. M. Wu, *Adv. Funct. Mater.* **2020**, *30*, 1907619.

[83] Y. J. Yuan, Z. K. Shen, S. T. Wu, Y. B. Su, L. Pei, Z. G. Ji, M. Y. Ding, W. F. Bai, Y. F. Chen, Z. T. Yu, Z. G. Zou, *Appl. Catal., B* **2019**, *246*, 120.

[84] Y. J. Yuan, Z. K. Shen, P. Wang, Z. J. Li, L. Pei, J. S. Zhong, Z. G. Ji, Z. T. Yu, Z. G. Zou, *Appl. Catal., B* **2020**, *260*, 118179.

[85] P. Kuang, L. Zhang, B. Cheng, J. G. Yu, *Appl. Catal., B* **2017**, *218*, 570.

[86] X. Y. Zhang, H. P. Li, X. L. Cui, Y. H. Lin, *J. Mater. Chem.* **2010**, *20*, 2801.

[87] Z. He, J. Fu, B. Cheng, J. G. Yu, S. Cao, *Appl. Catal., B* **2017**, *205*, 104.

[88] S. L. Shen, A. P. Ma, Z. H. Tang, Z. Han, M. J. Wang, Z. Wang, L. J. Zhi, J. H. Yang, *ChemCatChem* **2015**, *7*, 609.

[89] J. L. Xu, C. F. Sun, Z. Y. Wang, Y. D. Hou, Z. X. Ding, S. B. Wang, *Chem. - Eur. J.* **2018**, *24*, 18512.

[90] K. S. W. Sing, D. H. Everett, R. A. W. Haul, L. Moscou, R. A. Pierotti, J. Rouquerol, T. Siemieniewska, *Pure Appl. Chem.* **1985**, *57*, 603.